IEEE Access
Multidisciplinary | Rapid Review | Open Access Journal

SPECIAL SECTION ON IEEE POWER & ENERGY SOCIETY SECTION

Received 30 June 2025, accepted 8 July 2025, date of publication 11 July 2025, date of current version 17 July 2025.

Digital Object Identifier 10.1109/ACCESS.2025.3588109

RESEARCH ARTICLE

Edge-Fog Computing-Based Blockchain for Networked Microgrid Frequency Support

YING-YI HONG[1], (Senior Member, IEEE), FRANCISCO I. ALANO[1], YIH-DER LEE[2], (Member, IEEE), AND CHIA-YU HAN[2]

[1]Department of Electrical Engineering, Chung Yuan Christian University, Taoyuan City 32023, Taiwan
[2]National Atomic Research Institute, Taoyuan City 325207, Taiwan

Corresponding author: Ying-Yi Hong (yyhong@ee.cycu.edu.tw)

This work was supported in part by the National Atomic Research Institute under Grant NL1140089; in part by the National Science and Technology Council, Taiwan, under Grant NSTC 114-2218-E-033-001; and in part by Chung Yuan Christian University under Project CYCU-WIArk-250CH.

ABSTRACT Microgrids have gained increasing adoption in recent years due to the growing demand for renewable energy integration. Frequency support has become a critical issue in networked microgrid operation, primarily due to the intermittent nature of renewable energy sources and the inherently low system inertia of microgrids. Sudden system events, such as faults that lead to generator disconnections, can result in significant frequency drops. This paper proposes a novel method for providing frequency support during generator disconnection events in networked microgrids. The proposed approach integrates an edge–fog hierarchical blockchain architecture with a Long Short-Term Memory Model-Free Predictive Controller (LSTM-MFPC). The parameters and hyperparameters of the LSTM-MFPC are optimized using the Bayesian Adaptive Direct Search (BADS) algorithm. The root mean square error (RMSE) of the current obtained using the traditional model predictive control (MPC) and the proposed LSTM-MFPC applied to the inverter are 0.1970 and 0.1432, respectively. These results were obtained through experiments conducted on MATLAB/Simulink-based power hardware-in-the-loop (PHIL) platforms. This demonstrates that the proposed method significantly improves the frequency response of networked microgrids following fault events and exhibits strong potential for real-world implementation.

INDEX TERMS Bayesian adaptive direct search, edge device, energy blockchain, LSTM controller, model-free predictive controller.

I. INTRODUCTION

Renewable energy sources in the power grid have been increasing in number during the recent years. Resources such as wind turbines and solar panel arrays are increasingly being utilized as a common source of energy due to growing demand. Electricity is generated from these renewable sources by both large farms and smaller generators typically located in various areas. Unlike traditional power grids, which rely on large centralized generators, renewable energy is produced from multiple sources and locations within the power grid. This development has enabled the creation of microgrids, where energy producers are allowed to trade energy with each other or with the larger power grid. The distributed energy resources (DERs) are assigned specific roles within the microgrid, such as providing voltage and frequency regulation or supplying a designated amount of power [1]. Microgrids can be connected to or disconnected from the main grid depending on operational needs. When connected to the grid, excess energy can be sold to the utility, and electricity can be purchased when the microgrid's energy production is insufficient. This configuration is referred to as grid-connected mode. Conversely, microgrids can isolate themselves and rely entirely on their own energy producers, a configuration known as islanded mode. This setting is utilized when sufficient energy is produced within the

The associate editor coordinating the review of this manuscript and approving it for publication was Cuo Zhang.

microgrid, and disconnection from the main grid is deemed necessary to protect against external events, such as faults in the bulk power grid. This measure is taken to ensure stability and resilience, allowing continuous operation under normal conditions. Another method to enhance the resilience of microgrids is interconnection with other microgrids, forming networked microgrids. By interconnection, additional DERs are integrated into the system, providing resilience comparable to that of a traditional centralized power grid.

A. ENERGY BLOCKCHAIN STUDIES

The use of blockchain in power systems has been widely researched in recent years. Security has been identified as a major consideration for energy trading [2], leading to the development of algorithms designed to ensure the privacy of participants [3]. Blockchain networks have also been utilized to enable real-time bidding [4], which was employed to automatically maintain power balance or to restore frequency under disturbances [5], [6].

B. EDGE AND FOG COMPUTING STUDIES

Edge computing and Internet of things (IoT) devices have been utilized to facilitate the transition to smart grids. Security can be further enhanced by combining these technologies with blockchain, where multiple blockchains with specialized tasks are employed [7]. Data collected from these edge devices were used to train forecasting models that improved pricing models [8], which can be achieved through federated learning [9], [10]. The functionality of smart grids can also be further enhanced by incorporating a fog layer between the edge and the cloud, providing additional computational power to the network [11].

C. PREDICTIVE CONTROLLER STUDIES

Predictive controllers in power systems have been widely studied, particularly for controlling multiple distributed generators (DGs) in a microgrid. Model predictive controllers (MPCs) have been applied as centralized controllers in large-scale systems [12] and as secondary controllers for maintaining voltage and/or frequency stability [13], [14], [15], [16], [17]. MPCs have also been employed in the primary controllers of inverters for frequency control [18], [19], [20] and to ensure stability following fault occurrences [21]. Another approach to MPC is to replace the conventional MPC with data-driven models, such as artificial neural networks (ANNs), in order to reduce the computational burden on circuit-level controllers [22].

D. LIMITATIONS

The existing studies reviewed consist of several limitations that this study aims to improve upon:

(a) The majority of recent energy blockchain and edge computing literature has been focused primarily on the security of the network, while the real-time performance of the grid has not been extensively addressed [2], [3], [4], [9], [10], [11].
(b) Studies related to edge computing can be further improved with the addition of a fog layer [5], [9], [10].
(c) Studies related to the implementation of MPCs can be improved by adopting a model-free alternative to mitigate the limitations associated with reliance on an estimated model [12], [13], [14], [15], [16], [17], [18], [19], [20], [21], [22].
(d) The lack of hardware validation has resulted in the method's performance remaining unknown under real-world conditions [12], [13], [14], [15], [16], [17], [18], [19], [20], [21].

TABLE 1. Comparison between proposed method and recent works.

Reference	Application	Blockchain Algorithm	Edge/Fog	Controller
[5]	Electric Vehicle	Hyperledger Fabric	N/A	Synthetic Inertia Control
[9]	Cost optimization	N/A	Edge	N/A
[11]	Demand aggregation	N/A	Edge-Fog	N/A
[12]	Large scale distribution system control	N/A	N/A	Reconfigurable MPC
[13]	Islanded microgrid frequency control	N/A	N/A	Centralized MPC
[22]	Grid-tied inverter frequency control	N/A	N/A	ANN-based surrogate MPC
Proposed Method	Networked microgrid frequency control	PoS & Modified PoW	Edge-Fog	LSTM-MFPC

Table 1 presents a comparison between the proposed method and recent key works in the related literature.

E. MOTIVATIONS, PURPOSE AND CONTRIBUTIONS

This study aims to integrate blockchain and edge technology for frequency support in networked microgrids. The motivation for this study arises from the observation that only a few recent papers have leveraged edge devices for networked microgrid control, with most applications being limited as previously mentioned. Therefore, this paper seeks to combine these technologies to develop a hierarchical frequency support method for networked microgrids.

In this work, a long short-term memory model-free predictive controller (LSTM-MFPC) is proposed, to the best of our knowledge, for the first time as a secondary controller to enhance frequency recovery in networked microgrids during power interruptions. The LSTM-MFPC is designed to replace the conventional model predictive controller (MPC) and is deployed at the fog layer. Although LSTM-based and other data-driven controllers have previously been explored as alternatives to MPCs [22], this study uniquely employs the Bayesian Adaptive Direct Search (BADS) algorithm to

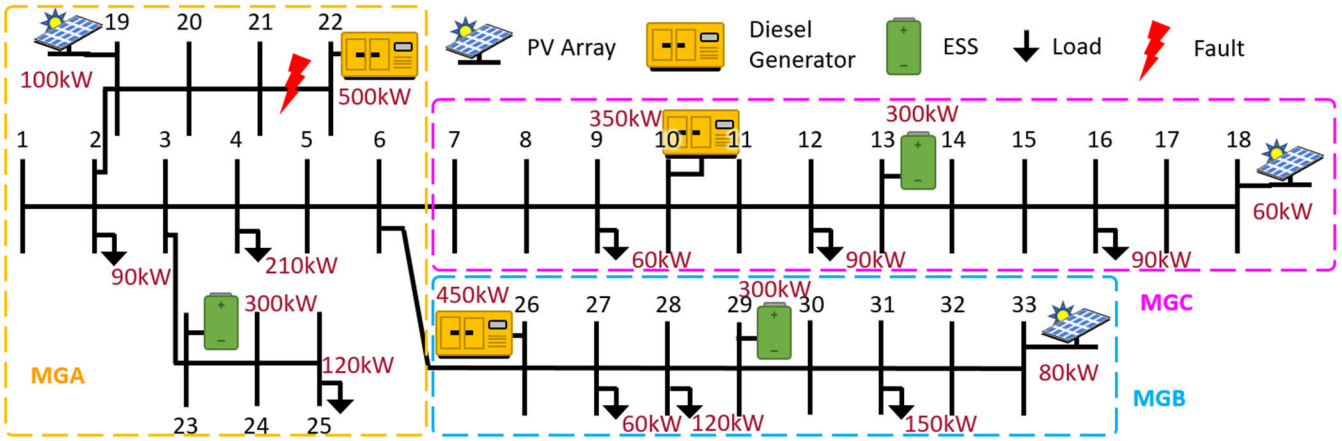

FIGURE 1. Modified IEEE 33-bus system.

optimize both the parameters and hyperparameters of the LSTM-MFPC, thereby ensuring its optimal performance. Simulation results demonstrate that the proposed controller achieves superior frequency response compared to conventional approaches. The contributions of the study are as follows:

(a) An edge-fog system is implemented to send and receive information from the grid, serve as nodes for participation in the blockchain network, and run a secondary controller for DGs in the networked microgrids.
(b) A two-blockchain system, deployed at the cloud and fog layers respectively, is designed to handle different tasks in the power grid. The blockchain on the cloud layer utilizes a conventional Proof-of-Stake (PoS) blockchain for handling transactions, while a modified Proof-of-Work (PoW) blockchain, specifically designed to work with a secondary controller, is deployed on the fog layer.
(c) A power hardware-in-the-loop (PHIL) simulation is conducted to validate the proposed method for real-world scenarios. The setup includes the use of an OPAL-RT real-time digital simulator, a converter circuit with a TI TMS320F28335 chip, and NVIDIA Jetson edge devices.

The rest of the research paper is structured as follows: Section II presents the problem description, which outlines the system used and the scenario that this study aims to address. Section III provides the background of the study, where the concepts employed are described in detail. Section IV explains how each component of the proposed method functions. Section V outlines the experimental setup, the results obtained, and the analysis of these results. Finally, Section VI presents the conclusions drawn from this study.

II. PROBLEM DESCRIPTION

In this section, the problem statement addressed by this study is presented. The test system is shown, along with the scenario in which the proposed method is implemented. The scope and assumptions of the experiment are described to ensure that the proposed method is tested under scenarios representative of real-world conditions.

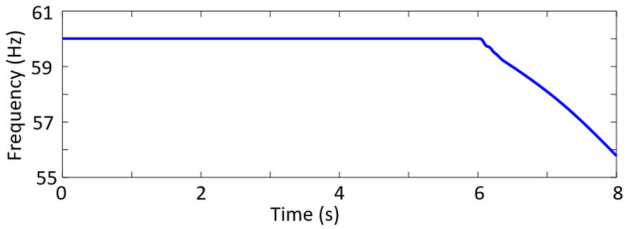

FIGURE 2. Frequency drop due to generator tripping.

A. SCOPE

The test system used in this study is based on a modified IEEE 33-bus system. It is disconnected from the main grid and subdivided into three microgrids (MGA, MGB, MGC), as shown in Fig. 1. Each microgrid is equipped with a diesel generator and a PV array of various ratings. A battery is connected to each microgrid and is configured to provide support when needed. Three loads with different power ratings (kW), drawing energy from the DGs, are connected to each microgrid. This test system was selected due to its frequent use in recent studies for investigating grid operation problems that simulate realistic conditions. The experiments involved in the study include the following:

(a) A 20-minute scenario is designed to test the edge-fog network with the two-blockchain system. This scenario is used to evaluate performance and confirm that proper transaction records are stored.
(b) Fifteen-second simulations are conducted under various scenarios to evaluate the performance of the proposed controller. In addition, PHIL testing is performed to validate the functionality of the edge–fog network with actual hardware and to assess the real-time response of the microgrid.

B. ASSUMPTIONS

The experimental setup includes tests in which the networked microgrids remain interconnected at all times, as well as a scenario in which the microgrids are initially islanded and then reconnected following a generator tripping event. Additional tests compare system performance under varying irradiance and load conditions, and include controllers drawn from related literature. These tests focus solely on frequency regulation, as low inertia is a well-known challenge due to inverter-based resources in microgrids and has been widely studied in the literature [23].

A fault is introduced in the system between buses 21 and 22, as shown in Fig. 1. This results in the tripping and disconnection of the diesel generator in MGA, causing a power imbalance. This imbalance leads to a frequency drop that needs to be mitigated. Fig. 2 shows the effect of the power imbalance, leading to the frequency drop.

Additional details about the test system are as follows:

(a) The PV arrays are set to maximum power point tracking (MPPT) control, ensuring that power output remains at its maximum at all times. The irradiance and temperature data used in this study are obtained from the Central Weather Administration of Taiwan [24].
(b) The load values are based on a typical 24-hour residential load data [25].
(c) The batteries are initially set to charge at 50 kW at the start of the simulation. The selection of the battery to provide power support is determined through the blockchain. Identical sizing and charging power are maintained to ensure a consistent initial condition for testing the controller.
(d) The diesel generators provide the remaining power required for each microgrid and do not always operate at maximum power output. The controllers of the diesel generators are designed to maintain the frequency at a constant 60 Hz. The power outputs of the diesel generators are not expected to change even after a fault is introduced in the system. Only the energy storage system (ESS) is expected to provide power support following the fault.

III. BACKGROUND OF STUDY

This section provides background concepts on the topics involved in formulating the proposed method. Each topic is explored to demonstrate how they can be combined for this study.

A. BLOCKCHAIN NETWORKS

Blockchain networks are digital ledgers used for storing information, as opposed to being stored on a single server. These blocks are encrypted using SHA-256 and become immutable once recorded, as shown in Fig. 3. Initially used for the cryptocurrency Bitcoin [26], blockchain can now also be applied to smart contracts, such as energy transactions.

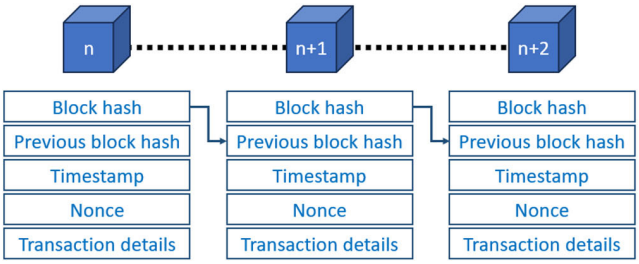

FIGURE 3. Blockchain structure.

Fig. 3 shows a basic blockchain structure and its contents. Each block contains data such as the timestamp and hash that prevent from tampering and maintains the chronological order of the chain. The nonce is a random number used to ensure the uniqueness of the block. The transaction details contain information such bidding and trading details in the case of an energy blockchain.

Blockchain networks can be classified in two ways: by consensus model or permission model. Various consensus models exist, with Proof of Work (PoW) and Proof of Stake (PoS) being the most common. PoW requires all participants to verify each block created in the blockchain, a process that is computationally complex and time-consuming. In contrast, PoS allows participants to stake assets in the network, and block creation is entirely dependent on the stakeholders. For permission models, there are public and private networks. Public networks are visible to all blockchain participants and are useful for ensuring transparency. Private blockchains, however, are only visible to selected users and are useful for storing sensitive information.

B. FOG AND EDGE COMPUTING

Edge devices are IoT devices that offload computation from cloud servers to avoid network congestion. These devices are referred to as ''edge'' devices because they are located at the ''edge'' of the network. They can be used to gather data or compute complex tasks locally, such as running neural networks. Additionally, these devices can serve as participants in a blockchain network for block creation. The capability of edge devices to gather, store, and send information can also be integrated with the power grid to create a smart grid.

Another layer, known as the fog, can also be added to the network between the edge and the cloud [27]. The devices used in this layer are the same as those in the edge layer, serving to further offload computations from both the cloud and edge. In the context of power systems, edge devices can be employed for each DG, while the fog layer can manage multiple DGs within a microgrid.

C. PREDICTIVE CONTROLLERS

Predictive controllers are a type of controller that can predict the state of the system. Unlike conventional proportional-integral-derivative (PID) controllers, which rely only on the measured error to adjust the output, a predictive controller

can estimate the future behavior of a system a few time steps ahead. This capability allows for better output performance in a plant under control.

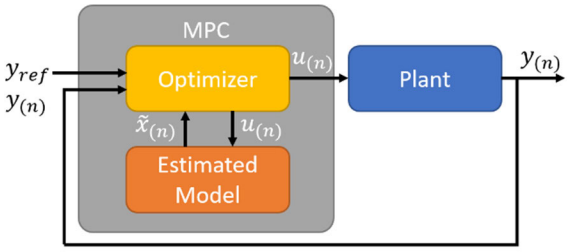

FIGURE 4. Model predictive controller.

One type of predictive control is model predictive control (MPC). In an MPC, an estimate of the system plant is created, usually through a state-space model, which is used to predict future states of the plant, as shown in Fig. 4. The measured output $y_{(n)}$ and reference value y_{ref} are fed into the optimizer. The optimizer then generates a control signal $u_{(n)}$ which is applied to both the plant and the estimated model block. This model block computes an estimated state $\tilde{x}_{(n)}$ which is returned to the optimizer. The updated plant output $y_{(n)}$ is also fed back to the optimizer, and the process is repeated iteratively.

Another type of predictive controller is the model-free predictive controller (MFPC), where the state-space model is replaced with a data-driven estimator, such as an LSTM, to predict the future states of the system. This eliminates the need for a computationally heavy real-time optimizer of a traditional MPC.

D. OPTIMIZATION ALGORITHMS

NN models contain parameters and hyperparameters that must be tuned properly to ensure optimal performance. One method for tuning these is to manually adjust each parameter or hyperparameter through trial and error, which is time-consuming and inefficient. A more efficient approach is to use optimization techniques. These techniques are mathematical algorithms designed to find an optimal combination of parameters and hyperparameters, such as particle swarm optimization (PSO) and Bayesian Optimization (BO). PSO utilizes multiple particles with different combinations of variables to search for a global maximum. In contrast, BO employs a stochastic approach with a surrogate model to create an estimate function, which is then used to systematically search for the global maximum. A modification of BO, known as the BADS, can be applied to improve optimization performance. BADS combines BO and mesh adaptive direct search (MADS) to enhance convergence speed and accuracy [28]. The algorithmic steps of BADS can be outlined below (Algorithm 1).

BADS works by evaluating the function s at the initial points z_0 and using BO to create a surrogate function at this point. After creating an estimate of the function in this area, the optimizer utilizes the MADS optimizer to find other potential locations of a global peak, adjusting the mesh size depending on the location of the possible minimum point. This process continues until a specific stopping criterion is met.

Algorithm 1 Bayesian Adaptive Direct Search

Inputs: objective function s, initial values z_0, lower bounds LB, upper bounds UB

Initialization: $\Delta_0^{mesh} \leftarrow 2^{-10}$, $\Delta_0^{poll} \leftarrow 0, j \leftarrow 0$,
evaluate s at initial values z_0
while stopping criteria are not fulfilled **do**
update Gaussian approximation
for $1 \ldots m_{search}$ **do** ▷ Local search
Determine z_{search} using BO
evaluate s on z_{search}
if improvement is *sufficient*, **break for**
if SEARCH IS NOT *successful* **then** ▷ Poll stage
compute poll set $Poll_j$
evaluate s on $Poll_j$ by acquisition function
if iteration j is *successful* **then**
$\Delta_j^{mesh} \leftarrow 2\Delta_j^{mesh}$, $\Delta_j^{poll} \leftarrow 2\Delta_j^{poll}$
else
$\Delta_j^{mesh} \leftarrow \frac{1}{2}\Delta_j^{mesh}$, $\Delta_j^{poll} \leftarrow \frac{1}{2}\Delta_j^{poll}$
$j \leftarrow j + 1$
check stopping conditions
return $s\left(z_{j(min)}\right)$

IV. PROPOSED METHOD

This section focuses on the proposed method to be implemented in this paper. Each component is described in detail, including its function and role in the power grid. The overall structure is then explained, describing how the entire method operates.

A. TWO-BLOCKCHAIN SYSTEM

The blockchain algorithms proposed in this study are a combination of a conventional PoS algorithm for handling transactions and a modified PoW algorithm designed for recording power measurements. The block diagram of the two blockchain is illustrated in Fig. 5.

The Transaction Blockchain is implemented as a private PoS blockchain, with the three microgrids serving as participants. Prior to a disturbance event, MGB and MGC submit bids to provide power support, and the bidder offering the lower price is selected. A block creation proposal is submitted to the Transaction Blockchain, where it must be validated by another participant. The probability p_m of a participant being selected as the validator in the Transaction Blockchain is defined in (1).

$$p_m = \frac{s_m c_m}{\sum_{m=1}^{M} s_m c_m} \tag{1}$$

Here, s_m denotes the staked amount, and c_m represents the coin age, defined as the duration for which the current stake

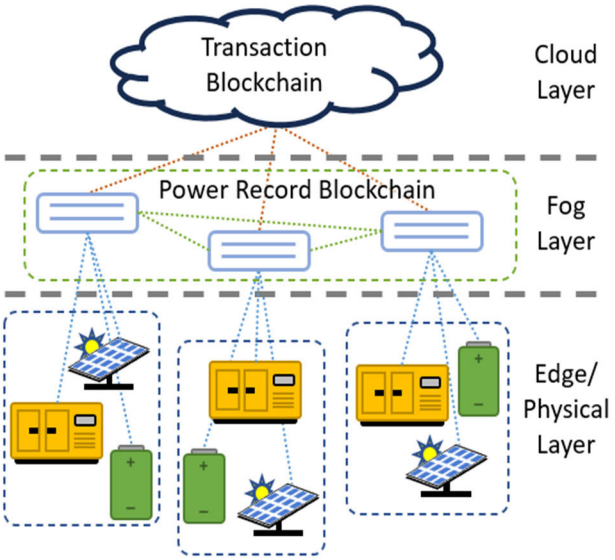

FIGURE 5. Data flow of the two-blockchain system.

has been held by microgrid m. The staked amount refers to the quantity of tokens that the participant owns in the blockchain network, while the coin age reflects the length of time the stake has been continuously held.

The Power Record Blockchain uses a modified PoW blockchain using the algorithm shown below (Algorithm 2).

Algorithm 2 Modified Proof-of-Work Algorithm

Initialization: DGs join Power Record Blockchain network
for every time step t **do**
  Get DG power measurements $P_{(t)}$ and frequency $F_{(t)}$
  Propose block creation $B_{(t)}$ by DG
  Run hash check by other DGs from same microgrid MG
  Run hash check by one random DG from another microgrid
  if 59.97 Hz $\leq F_{(t)} \leq$ 60.03 Hz
    Record as normal condition
  else
    Send support request to Transaction Blockchain
  end if
end for

This modified PoW algorithm enables all DGs and ESS to upload measurements to the system. To prevent data congestion, the consensus algorithm has been modified so that only the edge devices within the same microgrid and one randomly selected device from another microgrid are required to verify block creation. The inclusion of a random participant from a different microgrid helps maintain trust in the blockchain. This modification allows simultaneous uploading to the blockchain and reduces block creation time. Regarding scalability, the modified PoW algorithm is expected to perform consistently when additional microgrids are connected, due to the limited number of participants involved in the blockchain verification process.

The modified PoW algorithm reduces block creation time; however, it may pose a security risk due to the involvement of fewer participants. To address this limitation, a separate, more secure traditional PoS-based blockchain is used for bidding and transaction recording. Additionally, employing multiple blockchains within a single power system offers the advantage of improved record organization [29].

The blockchain programs are implemented in the Brownie framework, which allows Python to use Solidity and provides easy interfacing with both Simulink and Jetson devices.

B. EDGE-FOG HIERARCHICAL SYSTEM

A hierarchical system based on an edge–fog architecture is proposed in this study. An edge device is deployed for each distributed generator (DG) and battery unit within the grid. For each microgrid, a dedicated fog device is deployed and connected to the corresponding edge devices within that microgrid. A secondary controller is deployed on the fog layer, relying on the continuous stream of data from the edge devices. Each edge device uploads data to the fog layer, and the fog devices subsequently compute the total power of the networked microgrids. These devices are also responsible for computations necessary for the blockchain network, such as bidding, transactions, and block verification. The edge layer is responsible for obtaining power measurements from the DGs and the ESS. These measurements are uploaded to the Power Record Blockchain using Algorithm 2. These edge devices also allow to receive the control signal from the fog devices. Under normal conditions, the power records are directly uploaded to the blockchain. During fault conditions, the edge device that detects the generator trip sends a request to the fog layer for a bid. The bidding process is then executed by the fog devices to determine which microgrid will provide the power support. Each fog device receives the power measurements from the edge devices in its local microgrid. These fog devices then share the power measurements with each other and determine the amount of power needed to restore frequency. After the bidding, the fog device sends information back to the edge device that will be responsible for the power support. This fog device then activates the secondary controller to restore the frequency drop in the system.

C. LSTM MODEL-FREE PREDICTIVE CONTROLLER

An LSTM-based MFPC is proposed in this study as a replacement for the conventional MPC. The primary objective of this controller is to eliminate the requirement for a state-space model, which is typically needed in conventional MPC, by leveraging a data-driven approach based on LSTM networks.

Data for training the LSTM-MFPC is based on the hourly solar irradiance records provided by the Central Weather Administration of Taiwan from November 1, 2020, to November 30, 2022, which provides a total of 4051 usable data points. The dataset is divided into 60% for training,

20% for validation, and 20% for testing. The different data points provide different responses to the battery providing power support. These responses will be used to create a state-space model estimation using the following equations.

$$\tilde{x}_{(n)} = Ax_{(n)} + Bu_{(n)} \tag{2}$$
$$y_{(n)} = Cx_{(n)} + Du_{(n)} \tag{3}$$

where

A, B, C, D – state-space matrices
$x_{(n)}$ – state vector
$\tilde{x}_{(n)}$ – estimated state vector
$u_{(n)}$ – input
$y_{(n)}$ – output

The state-space matrices A, B, C, and D are estimated using the generated data for inputs and outputs. $u_{(n)}$ is the control action or plant input, while $y_{(n)}$ is the plant output at time step n using the proportional-integral (PI) controller. The identified state-space models for the bidirectional direct current (DC)-DC converter and inverter each have one manipulated variable, one output variable, and three states. For the bidirectional DC-DC converter, the MPC input is the DC bus voltage and the output is a dynamic reference DC bus voltage for the primary controller. For the inverter, the input is the Id (d-axis) current and the output is the dynamic Id current reference. MPC reference values for the DC bus voltage and Id current are calculated using the Power Record Blockchain. The block diagrams and additional details are shown in the appendix section.

The resulting state-space estimations are used for implementing the traditional MPC as a secondary controller. The block diagram for the secondary controller is shown in Fig. 6. In this configuration, the output measurement $y_{(n)}$ and the reference value y_{ref} serve as inputs to the optimizer. The optimizer generates a secondary control signal $v_{(n)}$, which is sent to the estimated model. The model provides state estimates back to the optimizer, enabling the computation of the optimal control action. The resulting command signal $v_{(n)}$ is then forwarded to the primary PI controller as its reference input. The PI controller compares this reference with the measured output $y_{(n)}$ and generates the primary control signal $u_{(n)}$, which is applied to the plant. The measured output $y_{(n)}$ is simultaneously fed back to both the primary and secondary controllers, and the control loop repeats.

Estimations are performed using the discrete-time state-space estimator in MATLAB. The MPC is implemented using Simulink and the responses for the 4051 scenarios are recorded for training the LSTM model.

The response curves of the traditional MPC are used for training the LSTM-MFPC controller. The LSTM architecture is shown in Fig. 7. The input variables used to train the LSTM model are derived from the conventional MPC, including the plant measurement $y_{(n)}$, the reference value y_{ref}, and the output of the secondary controller $v_{(n)}$. The LSTM generates internal states at each time step, consisting of the cell state

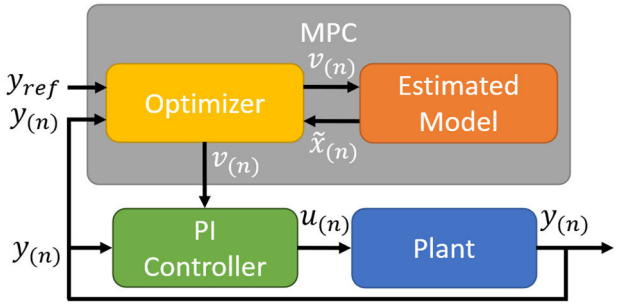

FIGURE 6. MPC secondary controller.

$C_{(n)}$ and the hidden state $h_{(n)}$. The hidden state $h_{(n)}$ is passed to the output layer, which computes the control signal $v_{(n)}$. To capture temporal dependencies, the model is trained using the past k values of both inputs and outputs. These recurrent connections enable the LSTM to utilize previous cell states $C_{(n)}$ and hidden states $h_{(n)}$ during training, enhancing its ability to model dynamic behavior.

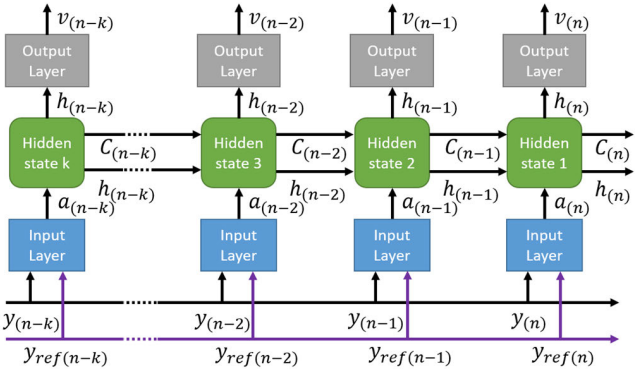

FIGURE 7. LSTM architecture.

Fig. 8 shows the block diagram of the proposed LSTM-MFPC method. Here, it is shown that the optimizer is removed and the state-space estimation is replaced with the LSTM model. The inputs to the proposed model are similar to those used in the conventional MPC, namely the output measurement $y_{(n)}$ and the reference value y_{ref}. However, unlike the MPC, the LSTM-based estimator replaces both the optimizer and the state-space model. The LSTM model directly outputs the command signal $v_{(n)}$, which is then sent to the primary PI controller.

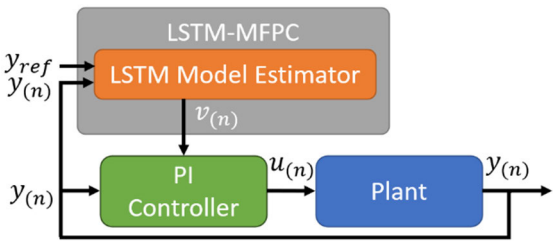

FIGURE 8. LSTM-MFPC block diagram.

D. BAYESIAN ADAPTIVE DIRECT SEARCH

The LSTM-MFPC models are tuned using the optimization algorithm to obtain the best parameter/hyperparameter combination for achieving optimal performance. The objective function of the optimization process is to minimize the mean absolute error (MAE) given in (4).

$$MAE = \frac{\sum_{n=1}^{N} \left| y_{ref\,(n)} - y_{(n)} \right|}{N} \tag{4}$$

where $y_{ref\,(n)}$ is the true value and $y_{(n)}$ is the predicted value at index n for a total of N sample points.

Different algorithms are tested on the LSTM-MFPC optimization to compare their performance in terms of convergence speed and final objective value. The BADS optimization is chosen for this paper as it has been proven in previous studies that this optimizer exhibits better performance in terms of convergence speed [30].

Table 2 shows the parameters and hyperparameters that will be optimized. The number of hidden states refers to the parameter in the LSTM that affects how many time steps are considered in the time series model. The learning rate affects the speed at which the weights and biases are adjusted during training, while the batch size refers to the number of samples considered during training. Both the learning rate and batch size are hyperparameters that influence the training of the model.

TABLE 2. Parameters and hyperparameters search space.

Parameter/Hyperparameter	Range
Hidden States	3 – 8
Learning Rate	0.0001 – 0.1
Batch Size	32 – 2048

E. OVERALL PROPOSED STRUCTURE

This subsection summarizes the individual components of the system and their interactions. First, the BADS algorithm is used exclusively during the design phase of the LSTM-MFPC for parameter and hyperparameter optimization. It is not involved in subsequent testing or deployment. Once training is complete, the optimized LSTM-MFPC is deployed on the fog device. Both the fog and edge devices participate in block creation within the proposed dual-blockchain architecture. Specifically, fog devices are responsible for creating and validating blocks in the Transaction Blockchain located at the cloud layer. During a generator trip event, the fog devices retrieve the bid-winning microgrid from the Transaction Blockchain to determine which microgrid will provide support. Meanwhile, edge devices are responsible for block creation in the Power Record Blockchain. These devices collect measurements from the DGs and use a modified PoW mechanism to upload the data to the blockchain. During a generator trip event, the edge devices also calculate the required power support and provide this value as the reference input to the LSTM-MFPC.

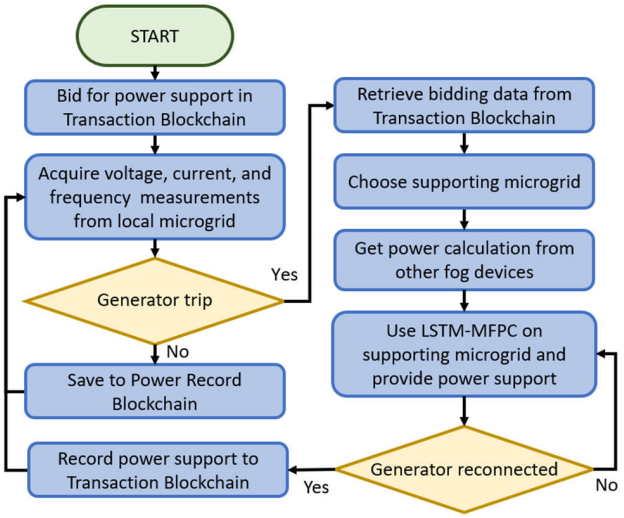

FIGURE 9. Proposed system process flowchart.

Fig. 9 illustrates the flowchart of the proposed method. Under normal conditions, power and frequency measurements are periodically recorded in the Power Record Blockchain. The presented modified PoW mechanism tracks each generator's power measurements and verifies frequency stability. If a generator trips, the modified PoW detects the frequency drop and triggers a bidding request to the Transaction Blockchain, initiating the selection process for a supporting microgrid. Once a supporting microgrid is determined, its secondary controller is activated. The required power, retrieved from the Power Record Blockchain, serves as the reference for the LSTM-MFPC. The battery in the selected microgrid restores frequency and provides continuous support until the generator reconnects to the microgrid.

Once the generator reconnects to the microgrid, power support ceases, and the secondary controller is deactivated. The battery in the microgrid resumes charging. The Transaction Blockchain records the total energy supplied and the associated cost during the power support period, after which the system returns to normal operation.

V. RESULTS AND DISCUSSION

A. CONVERGENCE PATTERN OF BAYESIAN OPTIMIZATION

The performance of the BADS algorithm is compared to BO and PSO by running each for the optimization of the two LSTM-MFPC models for the converter and inverter, respectively. The objective of the optimization is to minimize the MAE. The same parameter/hyperparameter search space, as shown in Table 2, is used by all three optimization algorithms.

The optimization algorithms are set to run a total of 350 function evaluations. All optimization algorithms use the same initial conditions: 5 hidden states, a learning rate of 0.001, and a batch size of 256.

All three optimization methods converge to similar MAE values—0.0213 for the bidirectional DC–DC converter and

0.0032 for the inverter controller. However, their convergence speeds differ. PSO demonstrates the slowest convergence, while BO converges faster than PSO. The BADS algorithm achieves the fastest convergence, requiring only 27 and 32 iterations for the converter and inverter, respectively. This observation is consistent with the optimization performance comparison reported in [30]. The optimized parameter and hyperparameter combinations obtained using BADS are summarized in Table 3.

TABLE 3. Optimized parameter/hyperparameter combination.

Bidirectional DC-DC Converter	
Parameter/Hyperparameter	**Value**
Hidden states	8
Learning rate	0.09803284
Batch size	1024
Inverter	
Parameter/Hyperparameter	**Value**
Hidden states	8
Learning rate	0.00133641
Batch size	256

B. ACCURACY COMPARISONS OF DIFFERENT CONTROLLERS

Fig. 10 shows the results of using a secondary MPC controller on the bidirectional DC-DC converter and inverter. A dynamic reference is provided by the MPC, which makes the measured values follow the desired reference value as close as possible.

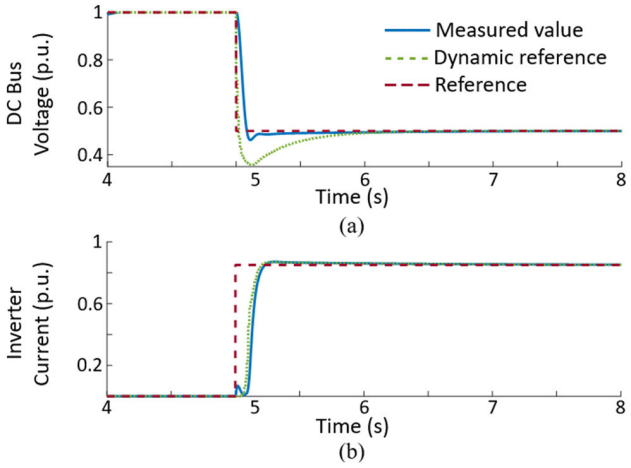

FIGURE 10. Dynamic reference provided by secondary MPC and primary control response for (a) bidirectional DC-DC converter and (b) inverter.

Four control methods are compared to one another in terms of performance. The first test involves using only a PI controller without a secondary controller. The second test uses the traditional MPC. The third and fourth tests involve two data-driven controllers—namely, a Multi-Layer Perceptron (MLP) and a Recurrent Neural Network (RNN)—as used in related literature [22]. The final test uses the proposed LSTM-MFPC controller. The results are compared in Fig. 11.

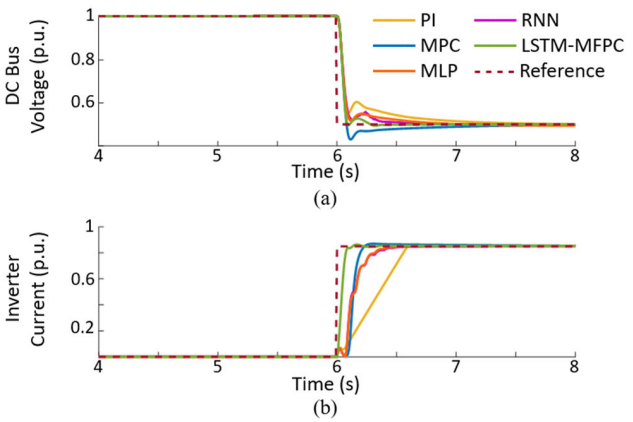

FIGURE 11. Offline simulation controller comparison.

It is observable in Fig. 11 that the MPC provides an advantage over using only a PI controller in terms of the system response where it is able to track the reference value faster. However, it also introduces a minor overshoot in both the bidirectional DC-DC converter voltage and the inverter current. Both the MLP and RNN controllers demonstrate a significant performance advantage over the conventional PI controller. The proposed LSTM-MFPC eliminates these overshoots, as well as to provide a faster response compared to both the PI and MPC.

The metrics used to evaluate the performance of the controllers are Mean Absolute Error (MAE), Root Mean Square Error (RMSE), and the coefficient of determination (R^2). These metrics are commonly employed in related literature for controller performance comparison [31]. The formula for MAE is provided in (4), while the formulas for RMSE and R^2 are presented in (5) and (6), respectively:

$$RMSE = \sqrt{\sum_{n=1}^{N} \frac{\left(y_{ref\,(n)} - y_{(n)}\right)^2}{N}} \tag{5}$$

$$R^2 = 1 - \frac{\sum_{n=1}^{N} \left(y_{ref\,(n)} - y_{(n)}\right)^2}{\sum_{n=1}^{N} \left(y_{ref\,(n)} - \overline{y_{ref\,(n)}}\right)^2} \tag{6}$$

where $\overline{y_{ref\,(n)}}$ denotes the mean of the N true values. The other symbols used in (5) and (6) are defined in Section IV-D.

Table 4 presents the error metrics done in the offline testing of the control methods. It can be seen from these results that the LSTM-MFPC provides the lowest MAE and RMSE as well as the highest R^2 value for both the bidirectional DC-DC converter and inverter.

Fig. 12 presents the frequency response under different control strategies. When only PI controllers are used without secondary controllers, the system experiences the worst frequency response. Implementing a conventional MPC in the secondary controller enables a better frequency response following a fault. The MLP and RNN controllers exhibit a response that is nearly identical to that of the conventional MPC. Among these methods, the proposed LSTM-MFPC achieves the best response.

TABLE 4. Comparison of controller error metrics.

	Bidirectional DC-DC converter			Inverter		
	MAE	RMSE	R^2	MAE	RMSE	R^2
PI	0.0209	0.0582	0.9555	0.0655	0.1952	0.7890
MPC	0.0151	0.0531	0.9613	0.0337	0.1468	0.8806
MLP	0.0109	0.0539	0.9542	0.0330	0.1398	0.8916
RNN	0.0128	0.0538	0.9543	0.0335	0.1406	0.8905
LSTM-MFPC	0.0094	0.0515	0.9634	0.0110	0.0747	0.9690

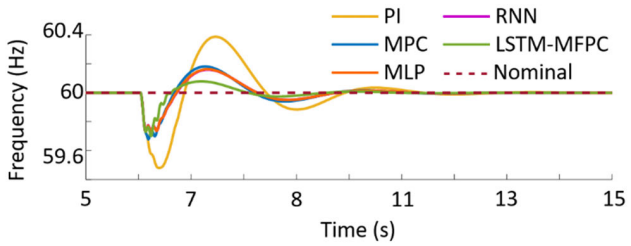

FIGURE 12. Frequency responses using different controllers (offline simulation).

Table 5 presents the frequency response metrics for the controllers evaluated in this test. The three metrics considered are nadir, overshoot, and settling time. The results indicate that the proposed LSTM-MFPC outperforms the other controllers generally. Although the MLP and RNN controllers exhibit slightly better nadir values, the LSTM-MFPC achieves superior performance in terms of overshoot and settling time compared to these data-driven approaches.

TABLE 5. Frequency response metrics.

	Nadir (Hz)	Overshoot (Hz)	Settling Time (s)
PI	59.4802	60.3878	5.1980
MPC	59.6786	60.1813	4.9338
MLP	59.7328	60.1600	4.9842
RNN	59.7304	60.1624	4.9774
LSTM-MFPC	59.7001	60.0791	4.5134

C. CONTROLLER TESTING UNDER VARYING PV POWER AND LOAD CONDITIONS

Different PV power and load conditions from the test dataset were considered in this subsection to validate the controller's performance. Table 6 presents the values of PV irradiance, temperature, and total load power (in per unit).

Fig. 13 illustrates the frequency responses obtained by the proposed LSTM-MFPC controller under varying conditions. Although differences are observed in terms of frequency drop, overshoot, and settling time, all responses remain within the acceptable frequency range of 59.7 Hz to 60.1 Hz [1].

D. CONTROLLER TESTING UNDER VARYING TIME DELAYS

The use of edge and fog devices introduces communication delays that may impact control performance. To validate the robustness of the proposed controller under such conditions, software simulations were conducted with varying time delays ranging from 0 ms to 25 ms. Fig. 14 presents the frequency responses of the proposed LSTM-MFPC controller under these delay scenarios, alongside a baseline case without delay. The results show that although communication latencies induce some oscillations in the response, the controller is still able to maintain the system frequency within the acceptable range.

TABLE 6. Varying PV power and load conditions.

Scenario	PV		Load
	Irradiance (W/m^2)	Temperature (°C)	Power (pu)
S1	210	21	0.208
S2	230	18	0.568
S3	210	29	0.878
S4	510	14	0.212
S5	500	27	0.568
S6	490	25	0.820
S7	1000	25	0.208
S8	990	26	0.568
S9	1000	25	0.878

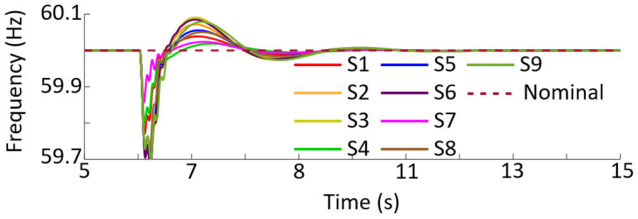

FIGURE 13. Frequency responses under varying PV and load conditions.

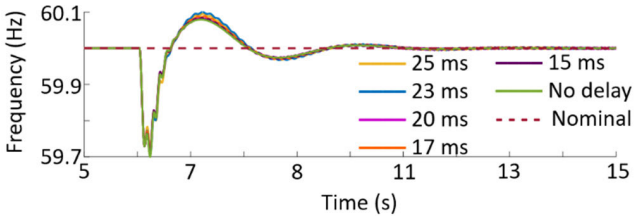

FIGURE 14. Frequency responses under varying time delays.

E. CONTROLLER TESTING FOR ISLANDED MICROGRIDS

Another scenario considered in this study involves islanded microgrid operation. As illustrated in Fig. 15, MGA is initially disconnected from the rest of the network. A fault is introduced between buses 19 and 20, resulting in the tripping of the PV array. Two simulation cases are conducted for comparison. In the first case, MGA restores its frequency independently using the diesel generator located at bus 22, without any interconnection. In the second case, MGB connects to MGA and provides power support. The frequency responses from both scenarios are compared and analyzed.

Fig. 16 presents a comparison of the frequency responses with and without support from MGB. As shown in Fig. 16,

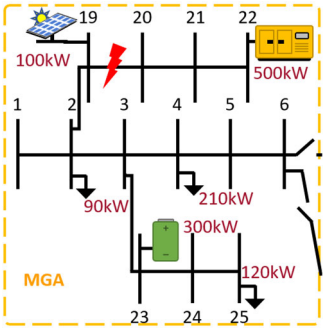

FIGURE 15. Islanded MGA scenario.

when MGA relies solely on its own diesel generator, the system experiences a greater frequency drop and a longer settling time compared to the scenario where a battery in the MGB provides power support.

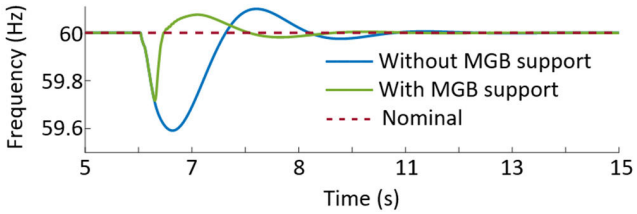

FIGURE 16. Frequency responses with and without MGB support.

F. BLOCKCHAIN OUTPUTS

The two-blockchain system is tested using the 20-minute simulation mentioned in Sec. II. This involves the use of both the Transaction Blockchain and the Power Record Blockchain. The Transaction Blockchain uses a conventional PoS, so the test focuses on whether it can successfully execute the bidding process among participants. An example of a bidding result is shown in Fig. 17.

```
Transaction Blockchain ready
*-------------------------------------------------------------------*
MGB bids 9.963 NTD/kWh
MGC bids 11.275 NTD/kWh
Bid winner: MGB
*-------------------------------------------------------------------*
Maximum Power: 391.3628460533502 kW
Total Energy provided: 462.7360974710153 kW-h
Earnings: 4610.239739103725 NTD
```

FIGURE 17. Transaction Blockchain output.

Fig. 17 shows a transaction that occurred between MGB and MGC. The bidding process shows that MGB offers a lower price, and is chosen to provide power/frequency support.

The Power Record Blockchain uses the modified PoW consensus and is compared to a conventional PoW in terms of block creation time. In a traditional PoW, all participants must verify the contents of a proposed block before it is approved for creation on the blockchain. In the proposed PoW, block verification relies on measurements from the networked microgrids, and only the participants within the same microgrid are required to check the block.

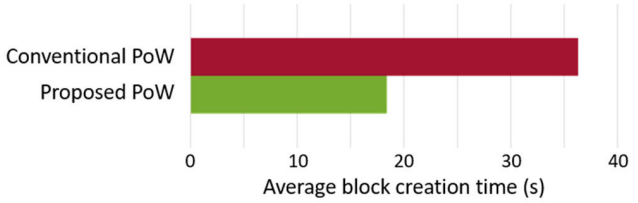

FIGURE 18. Average block authentication times of conventional PoW and proposed PoW.

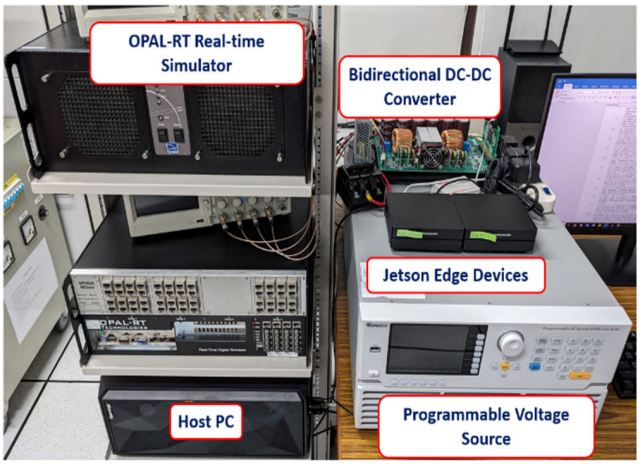

FIGURE 19. PHIL laboratory setup.

In Fig. 18, the conventional PoW and the proposed PoW are compared in terms of the average block creation time across a test of 100 blocks. The conventional PoW has an average block creation time of 36.3 seconds, while the proposed PoW reduces this to 18.4 seconds. This comparison demonstrates that the proposed method is well-suited for this application, as it allows for continuous updates of power records, which is essential for real-time application a smart grid.

G. POWER HARDWARE-IN-THE-LOOP (PHIL) OUTPUTS

A PHIL simulation is executed using the same scenario to validate the LSTM-MFPC controllers. The laboratory setup for this test is shown in Fig. 19. The setup includes the use of an OPAL-RT real-time digital simulator, a DC-DC converter with a TI TMS320F28335 chip, and NVIDIA Jetson edge devices.

A bidirectional DC-DC converter is tested to validate the performance of the LSTM-MFPC in an actual circuit. The onboard TI chip of the converter houses the primary PI controller. Similar to the offline testing conducted earlier, comparisons between three types of controllers are made. Two Jetson devices are connected via a LAN cable within a local network to assess whether the predictive controllers can handle the communication delay. One Jetson device serves as

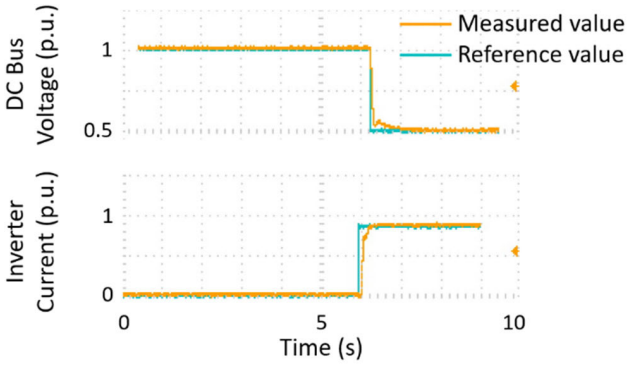

FIGURE 20. Oscilloscope outputs for LSTM-MFPC PHIL test.

TABLE 7. Error metrics for PHIL testing.

	Bidirectional DC-DC converter			Inverter		
	MAE	RMSE	R^2	MAE	RMSE	R^2
PI	0.0415	0.1065	0.9457	0.0724	0.2016	0.7801
MPC	0.0293	0.0993	0.9548	0.0732	0.1970	0.7901
LSTM-MFPC	0.0200	0.0965	0.9574	0.0338	0.1432	0.8890

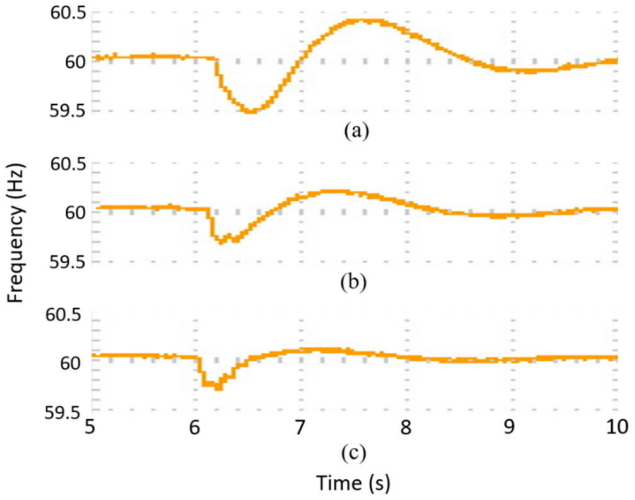

FIGURE 21. Oscilloscope outputs of frequency response obtained by (a) PI controller, (b) Conventional MPC, and (c) LSTM-MFPC.

the edge device, while the other functions as the fog device, where the secondary controller is deployed. Fig. 20 shows the oscilloscope output of the LSTM-MFPC controller. The error metrics from these tests are taken as well, as shown in Table 7.

The results indicate that the controller's performance during the PHIL tests is slightly lower than that observed in the offline simulations. This discrepancy is primarily attributed to the unknown communication latency inherent in the PHIL setup. Nevertheless, as demonstrated in the previous software-based tests (Section V-D), the proposed controller maintains stable operation under various latency conditions. Therefore, the PHIL results confirm the feasibility of implementing the proposed method on actual

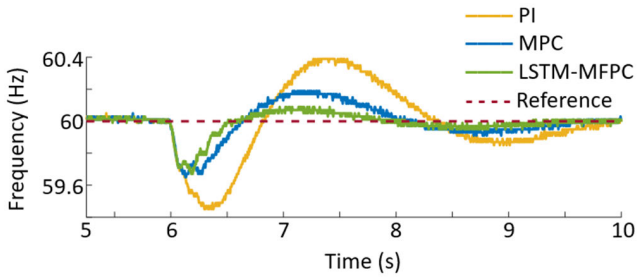

FIGURE 22. Oscilloscope outputs of frequency response comparison.

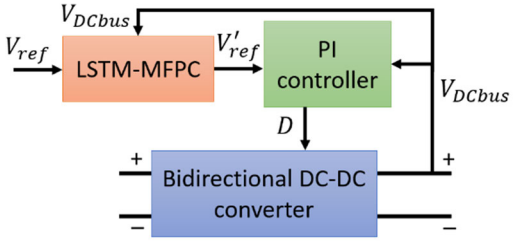

FIGURE 23. DC/DC converter and controller.

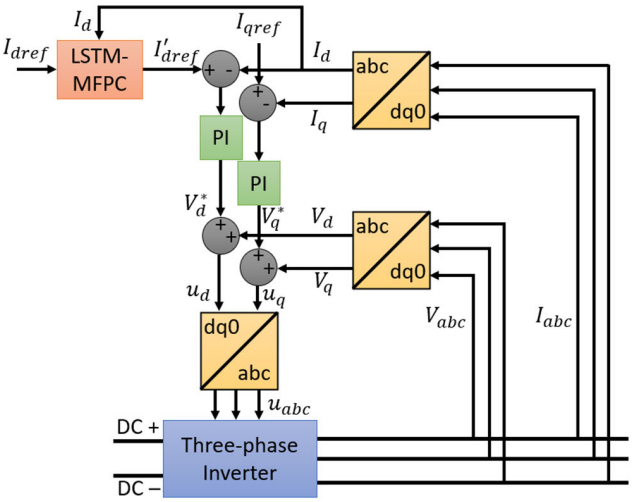

FIGURE 24. Inverter controller.

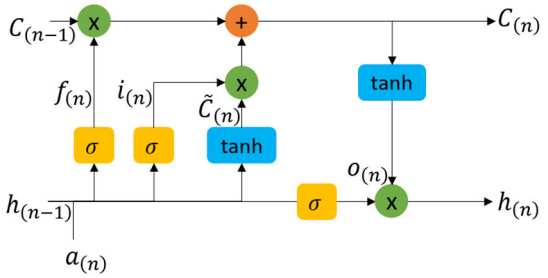

FIGURE 25. LSTM cell.

hardware for real-world applications. Fig. 21 shows the frequency response (oscilloscope outputs) of the networked microgrids when using only the primary controller and when

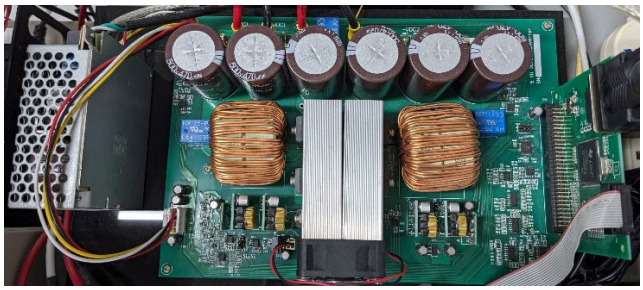

FIGURE 26. Bidirectional DC-DC converter.

FIGURE 27. Seeed Studio NVIDIA Jetson nano device.

adding the proposed LSTM-MFPC secondary controller. As shown in Fig. 21(a), with only the primary controller, the frequency drops to a lower value, and the settling time takes longer. In contrast, Fig. 21(b) illustrates the frequency response using the conventional MPC, demonstrating a lower frequency deviation and shorter settling time. Fig. 21(c) presents the response with the proposed LSTM-MFPC, achieving the fastest settling time with minimal overshoot. Fig. 22 is a consolidated graph combining the results from Fig. 21(a)–(c).

VI. CONCLUSION

This paper presents a method of combining blockchain technology and edge devices for providing frequency support in networked microgrids. A hierarchical system is implemented consisting of three levels: cloud, fog, and edge. Two scenarios were considered which include a 20-minute simulation and a 15-second simulation. A two-blockchain system is implemented which was proven to implement both a PoS algorithm as well as a modified PoW algorithm through the edge and fog devices. Multiple tests show that he proposed PoW method was able to create blocks in a shorter amount of time compared to the traditional PoW. Furthermore, it was shown to be able to work with a second blockchain deployed in the cloud through a fog network. In the 15-second simulation, a novel LSTM-MFPC was implemented to act a secondary controller to improve the frequency response of the system. In comparison to other control methods, it was proven that the LSTM-MFPC is superior compared to a traditional MPC in terms of response and controller overshoot. The model has been optimized through the BADS algorithm, which was shown to have a faster convergence speed compared with other optimization algorithms. The hardware tests show that the proposed method can be implemented on actual circuits and edge devices which proves the feasibility on real-world scenarios. Implementation of the proposed method requires the deployment of blockchain mechanisms and edge devices for each DG and battery. While this may increase system cost and introduce a requirement for continuous communication, integration with existing infrastructure is expected to be feasible, as traditional Supervisory Control And Data Acquisition (SCADA) and Energy Management Systems (EMS) are commonly used in microgrids.

Future studies will focus on implementing blockchain and edge computing technologies in larger-scale systems, such as the IEEE 69-bus network, involving a greater number of DGs and edge devices. In addition, unbalanced system conditions will be considered to further evaluate controller robustness. A major challenge in studying large-scale unbalanced systems lies in the computational limitations of the OPAL-RT digital simulator, particularly due to its limited core processing capacity. This issue may be addressed by employing parallel real-time simulation using interconnected multi-core and multi-CPU platforms.

APPENDIX A

Figs. 23 and 24 show the controllers for the bidirectional DC-DC converter and inverter, respectively. Both use PI controllers, with the only modification being that the reference values V'_{ref} and I'_{dref} are transmitted from the fog device, which is the variable $v_{(n)}$. I_{qref} is set to zero since reactive power/voltage support is not considered in this study. The fog device also receives the measured V_{DCbus} and I_d from the circuits, which correspond to the variable $y_{(n)}$, as shown in Fig. 8.

APPENDIX B

Fig. 25 shows the structure of the LSTM cell which forms each hidden state. The equations involved are as follows:

$$i_{(n)} = \sigma\left(a_{(n)}U^i + h_{(n-1)}W^i + b^i\right) \tag{7}$$

$$f_{(n)} = \sigma\left(a_{(n)}U^f + h_{(n-1)}W^f + b^f\right) \tag{8}$$

$$o_{(n)} = \sigma\left(a_{(n)}U^o + h_{(n-1)}W^o + b^o\right) \tag{9}$$

$$C_{(n)} = \sigma\left(f_{(n)} \odot C_{(n-1)} + i_{(n)} \odot \widetilde{C_{(n)}}U^i + b^c\right) \tag{10}$$

$$\widetilde{C_{(n)}} = \tanh\left(a_{(n)}U^g + h_{(n-1)}W^g\right) \tag{11}$$

$$h_{(n)} = \tanh\left(C_{(n)}\right) \odot o_{(n)} \tag{12}$$

where $i_{(n)}$ is the information control that affects the change of the cell state $C_{(n)}$, $f_{(n)}$ is the forget gate used to delete the current cell state, $\widetilde{C_{(n)}}$ is the possible replacement cell state, $a_{(n)}$ is the input matrix, $o_{(n)}$ is the output matrix, $h_{(n)}$ is the

short-term memory, U and W are the weights, and g and b are the biases.

APPENDIX C

This appendix provides the specifications of the bidirectional DC–DC converter and the Jetson-based edge devices used in this study.

Fig. 26 illustrates the circuit of the bidirectional DC–DC converter. The converter is controlled by a TI TMS320F28335 digital signal controller, which features a 150 MHz clock frequency, 512 kB of flash memory, and 68 kB of RAM. The board is equipped with an RS232-to-USB serial interface for communication with external devices.

Fig. 27 shows the hardware platform used for edge and fog-level testing. The device is a Seeed Studio reComputer J1010, equipped with an NVIDIA Tegra processor and 4 GB of onboard storage.

REFERENCES

[1] T. Basso, J. Hambrick, and D. DeBlasio, "Update and review of IEEE P2030 smart grid interoperability and IEEE 1547 interconnection standards," in *Proc. IEEE PES Innov. Smart Grid Technol. (ISGT)*, Jan. 2012, pp. 1–7.

[2] X. Zhou, B. Wang, Q. Guo, H. Sun, Z. Pan, and N. Tian, "Bidirectional privacy-preserving network-constrained peer-to-peer energy trading based on secure multiparty computation and blockchain," *IEEE Trans. Power Syst.*, vol. 39, no. 1, pp. 602–613, Jan. 2023.

[3] S. Zhang, Y. Zhang, and B. Wang, "Antiquantum privacy protection scheme in advanced metering infrastructure of smart grid based on consortium blockchain and RLWE," *IEEE Syst. J.*, vol. 17, no. 2, pp. 3036–3046, Feb. 2023.

[4] A. M. Saatloo, M. A. Mirzaei, and B. Mohammadi-Ivatloo, "A robust decentralized peer-to-peer energy trading in community of flexible microgrids," *IEEE Syst. J.*, vol. 17, no. 1, pp. 640–651, Mar. 2023.

[5] G. Sciumè, C. Iurlaro, S. Bruno, R. Musca, P. Gallo, G. Zizzo, E. R. Sanseverino, and M. L. Scala, "A blockchain-based architecture for tracking and remunerating fast frequency response," *Sustain. Energy, Grids Netw.*, vol. 40, Dec. 2024, Art. no. 101530.

[6] N. B. S. Shibu, A. R. Devidas, S. Balamurugan, S. Ponnekanti, and M. V. Ramesh, "Optimizing microgrid resilience: Integrating IoT, blockchain, and smart contracts for power outage management," *IEEE Access*, vol. 12, pp. 18782–18803, 2024.

[7] P. Wang, H. Li, H. Fu, Z. Sun, J. Chen, and X. Du, "A blockchain system for QoS monitoring in decentralized edge computing," *IEEE Trans. Services Comput.*, vol. 17, no. 1, pp. 263–276, Jan. 2024.

[8] S. Chavhan, D. Gupta, A. Alkhayyat, M. Alharbi, and J. J. P. C. Rodrigues, "AI-empowered game theoretic-enabled dynamic electric vehicles charging price scheme in smart city," *IEEE Syst. J.*, vol. 17, no. 4, pp. 5171–5182, Apr. 2023.

[9] H. Li, Y. Yang, Y. Liu, and W. Pei, "Federated dueling DQN based microgrid energy management strategy in edge-cloud computing environment," *Sustain. Energy, Grids Netw.*, vol. 38, Jun. 2024, Art. no. 101329.

[10] N. Abdulla, M. Demirci, and S. Ozdemir, "Smart meter-based energy consumption forecasting for smart cities using adaptive federated learning," *Sustain. Energy, Grids Netw.*, vol. 38, Jun. 2024, Art. no. 101342.

[11] H. R. Massrur, M. Fotuhi-Firuzabad, P. Dehghanian, and F. Blaabjerg, "Fog-based hierarchical coordination of residential aggregators and household demand response with power distribution Grids—Part II: Data transmission architecture and case studies," *IEEE Trans. Power Syst.*, vol. 40, no. 1, pp. 99–112, Jan. 2025.

[12] J. Chen, L. Zhang, and W. Gao, "Reconfigurable model predictive control for large scale distributed systems," *IEEE Syst. J.*, vol. 18, no. 2, pp. 965–976, Jun. 2024.

[13] T. Heins, M. Josevski, S. Karthik Gurumurthy, and A. Monti, "Centralized model predictive control for transient frequency control in islanded inverter-based microgrids," *IEEE Trans. Power Syst.*, vol. 38, no. 3, pp. 2641–2652, May 2023.

[14] Q. Yang, J. Zhou, X. Chen, and J. Wen, "Distributed MPC-based secondary control for energy storage systems in a DC microgrid," *IEEE Trans. Power Syst.*, vol. 36, no. 6, pp. 5633–5644, Nov. 2021.

[15] Z. Cheng, K. Wang, and Z. Li, "Distributed weighted average predictive control and delay margin analysis for an islanded microgrid with time delay," *Sustain. Energy, Grids Netw.*, vol. 39, Sep. 2024, Art. no. 101474.

[16] D. M. Rahman and S. Ganguly, "Voltage regulation and energy loss minimization for distribution networks with high photovoltaic penetration and EV charging stations using dual-stage model predictive control," *Sustain. Energy, Grids Netw.*, vol. 40, Dec. 2024, Art. no. 101529.

[17] F. Fachini, T. Bogodorova, L. Vanfretti, and S. Boersma, "A microgrid control scheme for islanded operation and re-synchronization utilizing model predictive control," *Sustain. Energy, Grids Netw.*, vol. 39, Sep. 2024, Art. no. 101464.

[18] O. Stanojev, U. Markovic, P. Aristidou, G. Hug, D. Callaway, and E. Vrettos, "MPC-based fast frequency control of voltage source converters in low-inertia power systems," *IEEE Trans. Power Syst.*, vol. 37, no. 4, pp. 3209–3220, Jul. 2022.

[19] X. Liu, C. Wang, X. Kong, Y. Zhang, W. Wang, and K. Y. Lee, "Tube-based distributed MPC for load frequency control of power system with high wind power penetration," *IEEE Trans. Power Syst.*, vol. 39, no. 2, pp. 3118–3129, Feb. 2023.

[20] Z. Hu, B. Gao, and R. Sun, "An active primary frequency regulation strategy for grid integrated wind farms based on model predictive control," *Sustain. Energy, Grids Netw.*, vol. 32, Dec. 2022, Art. no. 100955.

[21] A. Arjomandi-Nezhad, Y. Guo, B. C. Pal, and D. Varagnolo, "A model predictive approach for enhancing transient stability of grid-forming converters," *IEEE Trans. Power Syst.*, vol. 39, no. 5, pp. 6675–6688, Sep. 2024.

[22] P. Ranjan Bana, M. Amin, and M. Molinas, "ANN-based surrogate PI and MPC controllers for grid-connected VSC system: Small-signal analysis and comparative evaluation," *IEEE J. Emerg. Sel. Topics Power Electron.*, vol. 12, no. 1, pp. 566–578, Feb. 2024, doi: 10.1109/JESTPE.2023.3328260.

[23] W. Liu, G. Geng, Q. Jiang, H. Fan, and J. Yu, "Model-free fast frequency control support with energy storage system," *IEEE Trans. Power Syst.*, vol. 35, no. 4, pp. 3078–3086, Jul. 2020.

[24] (2024). *Central Weather Administration*. Accessed: Jun. 16, 2025. [Online]. Available: https://www.cwa.gov.tw/eng/

[25] D. Q. Hung, N. Mithulananthan, and K. Y. Lee, "Determining PV penetration for distribution systems with time-varying load models," *IEEE Trans. Power Syst.*, vol. 29, no. 6, pp. 3048–3057, Nov. 2014, doi: 10.1109/TPWRS.2014.2314133.

[26] S. Nakamoto. (2025). *Bitcoin: A Peer-to-Peer Electronic Cash System*. Accessed: Jan. 9, 2025. [Online]. Available: https://bitcoin.org/bitcoin.pdf

[27] G. Gao, C. Song, T. G. T. A. Bandara, M. Shen, F. Yang, W. Posdorfer, D. Tao, and Y. Wen, "FogChain: A blockchain-based peer-to-peer solar power trading system powered by fog AI," *IEEE Internet Things J.*, vol. 9, no. 7, pp. 5200–5215, Apr. 2022.

[28] L. Acerbi and W. Ji, "Practical Bayesian optimization for model fitting with Bayesian adaptive direct search," in *Proc. Adv. Neural Inf. Process. Syst.*, vol. 30, Dec. 2017, pp. 1834–1844.

[29] A. S. Musleh, G. Yao, and S. M. Muyeen, "Blockchain applications in smart Grid–Review and frameworks," *IEEE Access*, vol. 7, pp. 86746–86757, 2019.

[30] Q.-H. Feng, S.-S. Li, X.-M. Zhang, X.-F. Gao, and J.-H. Ni, "Well production optimization using streamline features-based objective function and Bayesian adaptive direct search algorithm," *Petroleum Sci.*, vol. 19, no. 6, pp. 2879–2894, Dec. 2022.

[31] F. Liu, Y. Peng, Q. Liu, H. Li, K. Liu, and Y. Peng, "Mode identification-based model-free adaptive predictive damping control method for power system with wind farm considering communication delays," *Int. J. Electr. Power Energy Syst.*, vol. 162, Nov. 2024, Art. no. 110303.

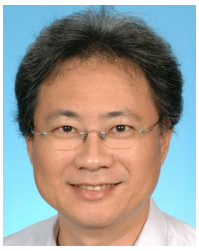

YING-YI HONG (Senior Member, IEEE) received the B.S.E.E. degree from Chung Yuan Christian University (CYCU), Taiwan, in 1984, the M.S.E.E. degree from National Cheng Kung University (NCKU), Taiwan, in 1986, and the Ph.D. degree from the Department of Electrical Engineering, National Tsing-Hua University (NTHU), Taiwan, in December 1990. Sponsored by the Ministry of Education, Taiwan, he conducted research with the Department of Electrical Engineering, University of Washington, Seattle, WA, USA, from August 1989 to August 1990. Since 1991, he has been with CYCU. He was the Dean of the College of Electrical Engineering and Computer Science, CYCU, from 2006 to 2012. From 2012 to 2018, he was a Secretary General with CYCU, where he is currently the Vice President and a Chair Professor. His research interests include power system analysis and artificial intelligence applications. He received the Outstanding Professor of Electrical Engineering Award from the Chinese Institute of Electrical Engineering (CIEE), Taiwan, in 2006. He was the Chair of the IEEE PES Taipei Chapter, in 2001.

FRANCISCO I. ALANO received the bachelor's degree in electronics engineering from Adamson University, Manila, in 2016. He is currently pursuing the master's and Ph.D. degrees with Chung Yuan Christian University, Taiwan. His research interest includes energy blockchain.

YIH-DER LEE (Member, IEEE) received the Ph.D. degree in electrical engineering from National Sun Yat-sen University, Kaohsiung, Taiwan, in 2009. From 1998 to 2010, he was an Associate Technical Specialist with the Southern District Waste Management Plant, Environment Protection Bureau, Kaohsiung City Government, Taiwan. In 2010, he joined the National Atomic Research Institute. He is currently the Director responsible for developing smart grid technology. His research interests include renewable energy, microgrids, power electronics, power system control, and stability.

CHIA-YU HAN received the Ph.D. degree in electrical engineering from the National Taipei University of Technology, in 2013. He is currently an Assistant Researcher with the National Atomic Research Institute. His research interests include power system fault analysis, protection coordination, and real-time simulation.